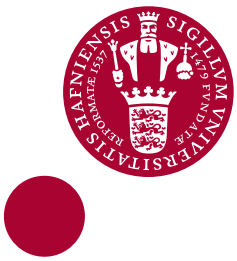

Learning from oligosaccharide soaks of crystals of an AA13 lytic polysaccharide monooxygenase

crystal packing, ligand binding and active-site disorder

Frandsen, Kristian Erik Høpfner; Poulsen, Jens-Christian Navarro; Tovborg, Morten; Johansen, Katja Salomon; Lo Leggio, Leila

Published in:
Acta crystallographica Section D: Structural biology

DOI:
10.1107/S2059798316019641

Publication date:
2017

Document version
Publisher's PDF, also known as Version of record

STRUCTURAL BIOLOGY

ISSN: 2059-7983
journals.iucr.org/d

Learning from oligosaccharide soaks of crystals of an AA13 lytic polysaccharide monooxygenase: crystal packing, ligand binding and active-site disorder

Kristian E. H. Frandsen, Jens-Christian Navarro Poulsen, Morten Tovborg, Katja S. Johansen and Leila Lo Leggio

Acta Cryst. (2017). D**73**, 64–76

STRUCTURAL BIOLOGY
ISSN 2059-7983

Learning from oligosaccharide soaks of crystals of an AA13 lytic polysaccharide monooxygenase: crystal packing, ligand binding and active-site disorder

Kristian E. H. Frandsen,[a] Jens-Christian Navarro Poulsen,[a] Morten Tovborg,[b] Katja S. Johansen[c] and Leila Lo Leggio[a]*

[a]Department of Chemistry, University of Copenhagen, Universitetsparken 5, 2100 Copenhagen, Denmark, [b]Novozymes A/S, Krogshoejvej 36, 2880 Bagsvaerd, Denmark, and [c]Department of Geoscience and Natural Resource Management, University of Copenhagen, Rolighedsvej 23, Frederiksberg C, 1958 Copenhagen, Denmark. *Correspondence e-mail: leila@chem.ku.dk

Received 5 September 2016
Accepted 8 December 2016

Edited by Z. S. Derewenda, University of Virginia, USA

Keywords: lytic polysaccharide monooxygenases; LPMOs; starch degradation; active-site stability; biomass utilization.

PDB references: Zn-*Ao*AA13, 5t7j; *Ao*AA13-His91flip, 5t7k; *Ao*AA13-G2(α1,4), 5lsv; *Ao*AA13-G3(α1,4)G1(α1,6), 5t7n

Supporting information: this article has supporting information at journals.iucr.org/d

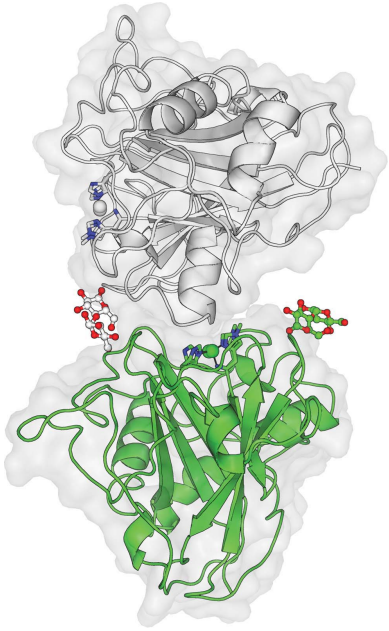

Lytic polysaccharide monooxygenases (LPMOs) are a class of copper-dependent enzymes discovered within the last ten years. They oxidatively cleave polysaccharides (chitin, lignocellulose, hemicellulose and starch-derived), presumably making recalcitrant substrates accessible to glycoside hydrolases. Recently, the first crystal structure of an LPMO–substrate complex was reported, giving insights into the interaction of LPMOs with β-linked substrates (Frandsen *et al.*, 2016). The LPMOs acting on α-linked glycosidic bonds (family AA13) display binding surfaces that are quite different from those of LPMOs that act on β-linked glycosidic bonds (families AA9–AA11), as revealed from the first determined structure (Lo Leggio *et al.*, 2015), and thus presumably the AA13s interact with their substrate in a distinct fashion. Here, several new structures of the same AA13 enzyme, *Aspergillus oryzae* AA13, are presented. Crystals obtained in the presence of high zinc-ion concentrations were used, as they can be obtained more reproducibly than those used to refine the deposited copper-containing structure. One structure with an ordered zinc-bound active site was solved at 1.65 Å resolution, and three structures from crystals soaked with maltooligosaccharides in solutions devoid of zinc ions were solved at resolutions of up to 1.10 Å. Despite similar unit-cell parameters, small rearrangements in the crystal packing occur when the crystals are depleted of zinc ions, resulting in a more occluded substrate-binding surface. In two of the three structures maltooligosaccharide ligands are bound, but not at the active site. Two of the structures presented show a His-ligand conformation that is incompatible with metal-ion binding. In one of these structures this conformation is the principal one (80% occupancy), giving a rare atomic resolution view of a substantially misfolded enzyme that is presumably rendered inactive.

1. Introduction

Lytic polysaccharide monooxygenases (LPMOs) are a class of copper-containing metalloenzymes that are able to oxidatively cleave polysaccharides by oxidizing the pyranose units at C1 and/or C4. They have been found to act in synergy with glycoside hydrolases (GHs; Harris *et al.*, 2010) in the degradation of polysaccharides and therefore have great potential use in the utilization of biomass (Johansen, 2016; Hemsworth *et al.*, 2015). They possess a central β-sandwich core and an active site consisting of the N-terminal histidine and an internal histidine, termed the histidine brace (Quinlan *et al.*, 2011; hereafter referred to as the His brace), which coordinates a copper ion. The N-terminal histidine is often found to be N^{ε}-methylated in fungi. The first LPMO structures showed

no obvious substrate-binding grooves as are commonly seen for GHs (Vaaje-Kolstad *et al.*, 2005; Karkehabadi *et al.*, 2008; Lo Leggio *et al.*, 2012). The substrate has been found to interact with the active site on a rather flat surface (Aachmann *et al.*, 2012; Courtade *et al.*, 2016) that may contain aromatic residues proposed to mediate substrate interactions (Harris *et al.*, 2010; Li *et al.*, 2012). The first LPMOs discovered were found to act on cellulosic substrates (Beeson *et al.*, 2012; Quinlan *et al.*, 2011) or chitin (Vaaje-Kolstad *et al.*, 2010), and are now classified in the CAZy database (Lombard *et al.*, 2014) as enzymes with auxiliary activity (AA; created after Levasseur *et al.*, 2013) in the families AA9 (formerly GH61) and AA10 (formerly CBM33). An additional chitin-active family was later identified (AA11, defined after Hemsworth *et al.*, 2014).

Later, structures of AA9s that are active on soluble oligosaccharides [from *Neurospora crassa* (*Nc*AA9C) and *Lentinus similis* (*Ls*AA9A)] showed a slightly more contoured substrate-interacting surface than had been observed in the first AA9 structures (Frandsen *et al.*, 2016; Borisova *et al.*, 2015). For AA9, substrate interaction at the proposed binding surface (and the involvement of a conserved aromatic residue in AA9) was categorically confirmed with *Ls*AA9A, as the structure was solved in complex with cellooligosaccharides (Frandsen *et al.*, 2016). *Ls*AA9A was the first LPMO–carbohydrate complex crystal structure to be published, thus yielding insight into the LPMO–substrate interactions at this interface and the general LPMO mode of action. The exact catalytic mechanism is still not certain and possible mechanisms used by LPMOs have been discussed in recent reviews (Lee & Karlin, 2015; Hemsworth *et al.*, 2015; Walton & Davies, 2016).

Recently, a family of starch-degrading LPMOs was discovered, which has now been classified as family AA13 in the CAZy database. These starch-degrading LPMOs were first described in patent literature as having amylolytic-enhancing activity (Harris & Wogulis, 2010) and were later demonstrated to be LPMOs (Vu *et al.*, 2014). The first structural characterization of a member of the family came in 2015 for an LPMO from *Aspergillus oryzae* (Lo Leggio *et al.*, 2015; hereafter denoted *Ao*AA13). The published structure (Cu-*Ao*AA13) has copper bound at the active site, and displayed a shallow groove at the putative substrate-binding surface instead of the flat surface commonly seen for all earlier LPMOs structures. Recently, a review has been published highlighting the major impact of structural studies in the investigation of LPMOs (Frandsen & Lo Leggio, 2016).

Until the present study, no complexes of LPMOs with α-linked substrates were available. In the *Ao*AA13 publication (Lo Leggio *et al.*, 2015), activity was shown for a highly sequence-related AA13 member from *Aspergillus nidulans* (*An*AA13) linked to a CBM20 (carbohydrate-binding module family 20), a CBM family characteristic of starch binding (Janeček *et al.*, 2011; Christiansen *et al.*, 2009). Members of family AA13 are often linked to CBM20, and these CBMs have been shown to bind starch substrates with affinities similar to those of the CBM20 associated with amylolytic hydrolases (Nekiunaite *et al.*, 2016). *An*AA13 releases C1-oxidized maltooligosaccharides [with a degree of polymerization (DP) of >4] from retrograded starch in the presence of reducing cofactors. A 100-fold increased release of maltose from retrograded starch by β-amylases was also demonstrated in the presence of *An*AA13. Activity on starch-related substrates (including corn starch, amylose, amylopectin and maltodextrins) was additionally reported for an AA13 from *N. crassa* (*Nc*AA13; Vu *et al.*, 2014), for which the authors even speculated that some of the products originated from C1-oxidation of the α-1,6 linkages found in amylopectin. For another AA13 from *Aspergillus terreus* (*At*AA13), activity has been demonstrated indirectly (Nekiunaite *et al.*, 2016) by inhibition of the Amplex Red assay (Kittl *et al.*, 2012) in the presence of β-cyclodextrin and amylose (DP of $\sim$17).

*Ao*AA13, in contrast to *An*AA13, *Nc*AA13 and *At*AA13, is a single-domain enzyme and, although no detectable activity could be measured for *Ao*AA13 (Lo Leggio *et al.*, 2015), the catalytic domain shares as much as 70–72% sequence identity with those of *An*AA13, *Nc*AA13 and *At*AA13. Here, we present our attempts to obtain catalytically relevant crystallographic complexes of *Ao*AA13 by soaking of maltooligosaccharides, the unexpected changes in local packing that we observed in the course of these experiments, and the implications for active-site accessibility. We nonetheless obtained high-resolution structures of *Ao*AA13 interacting with small maltooligosaccharides at distal binding sites and we discuss their possible biological implications. We also present structures with a remarkably misfolded active site. In these structures, the active site adopts a non-native conformation that is incapable of coordinating the active-site metal, thus presumably rendering the enzyme completely inactive.

2. Materials and methods

2.1. Macromolecule production

*Ao*AA13 production was as described in US patent application US 2011/0283421 (Harris & Wogulis, 2010, 2011). Details of expression and purification are also provided in Lo Leggio *et al.* (2015). For additional information, see Supplementary Table S1.

2.2. Crystallization

Screening for crystallization conditions was performed in MRC 2-drop crystallization plates (Molecular Dimensions) by setting up 0.3 µl drops (with protein:reservoir ratios of 3:1 and 1:1) using an Oryx8 robot (Douglas Instruments). Initial crystal hits were obtained with 6 mg ml^{-1} protein in (i) 10%(*w*/*v*) PEG 3000, 0.2 *M* zinc acetate, 0.1 *M* sodium acetate pH 4.5 and (ii) 20%(*w*/*v*) PEG 3000, 0.2 *M* zinc acetate, 0.1 *M* imidazole pH 8.0, both from the JCSG+ Suite (Qiagen; Supplementary Figs. S1*a* and S1*b*). Crystals were reproducible with 2.4–6.0 mg ml^{-1} protein in a range of 6–14%(*w*/*v*) PEG 3000 at pH 4.5 or in a range of 16–24%(*v*/*v*) PEG 3000 at pH 8.0. Because of the wide pH range in the otherwise similar conditions, optimization were performed on the basis of pH by

Table 1
Data-collection statistics.

Values in parentheses are for the outer shell.

	Zn-*Ao*AA13 (unliganded)	*Ao*AA13-His91flip	*Ao*AA13-G2(α1,4)	*Ao*AA13-G3(α1,4)G1(α1,6)
Diffraction source	ID14-4, ESRF	I911-3, MAX-lab	I911-3, MAX-lab	I911-3, MAX-lab
Wavelength (Å)	0.9334	1.0000	1.0000	0.9999
Temperature (K)	100	100	100	100
Detector	CCD	CCD	CCD	CCD
Crystal-to-detector distance (mm)	180.57	120.00	79.77	160.00
Rotation range per image (°)	1.0	1.0	0.5	1.0
Total rotation range (°)	180.0	200.0	193.5	180.0
Space group	$P2_12_12_1$	$P2_12_12_1$	$P2_12_12_1$	$P2_12_12_1$
a, *b*, *c* (Å)	47.04, 61.49, 73.79	45.56, 59.08, 71.76	45.40, 58.84, 71.90	45.67, 59.00, 72.15
α, β, γ (°)	90, 90, 90	90, 90, 90	90, 90, 90	90, 90, 90
Mosaicity (°)	0.143	0.107	0.163	0.409
Resolution range (Å)	30.00–1.65 (1.72–1.65)	30.00–1.30 (1.37–1.30)	30.00–1.10 (1.13–1.10)	30.00–1.60 (1.64–1.60)
Total No. of reflections	173493 (11020)	357103 (29842)	586098 (38851)	179873 (7069)
No. of unique reflections	26074 (2741)	47483 (6401)	78799 (5751)	26328 (1888)
Completeness (%)	98.7 (90.2)	98.2 (92.3)	99.9 (99.9)	99.7 (96.9)
Multiplicity	6.65 (4.02)	7.52 (4.66)	7.44 (6.76)	6.83 (3.74)
$\langle I/\sigma(I)\rangle$	17.96 (2.11)	17.81 (3.59)	13.37 (2.99)	21.14 (3.14)
R_{meas} (%)	8.8 (70.6)	8.2 (43.3)	12.9 (90.0)	7.5 (45.6)
$CC_{1/2}$ (%)	99.9 (71.3)	99.9 (86.2)	99.9 (83.3)	99.9 (85.8)
Overall *B* factor from Wilson plot† (Å^2)	22.88	13.21	9.00	19.39

† Calculated using *SFCHECK* in the *CCP*4 suite.

changing to buffer system II (a buffer system consisting of a 1:2:2 molar ratio of malic acid:MES:Tris) as described elsewhere (Newman, 2004). The crystals were also found to be reproducible with 20%(*w*/*v*) PEG 3000, 0.2 *M* zinc acetate when varying the pH from 4.0 to 9.0 with buffer system II (Supplementary Fig. S1*c*). Crystals were further optimized by setting up VDX plates with microseeding. The optimized conditions were 20%(*w*/*v*) PEG 3000, 0.1 *M* buffer system II pH 5.0, 0.2 *M* zinc acetate and 2.0–3.0 mg ml^{-1} protein solution in a ratio of 3.0 µl protein solution to 1.0 µl reservoir solution followed by immediate streak-seeding (Fig. 1).

From these crystals, a seed stock with reduced zinc content was made [by transferring crystals into a solution consisting of solely 20%(*w*/*v*) PEG 3000 and crushing them]. The seed stock was used in a microseed matrix-screening approach along with protein sample pre-incubated for 1 h with 1 m*M* copper(II) acetate (as described in Lo Leggio *et al.*, 2015, and references therein). Crystals appeared in a condition devoid of zinc [14%(*v*/*v*) 2-propanol, 30%(*v*/*v*) glycerol, 0.14 *M* $CaCl_2$, 0.07 *M* sodium acetate pH 4.6] and, from these, the Cu-*Ao*AA13 structure (Lo Leggio *et al.*, 2015) was determined. Unfortunately, this procedure was not very reproducible and the method was deemed to be unsuitable for the production of a large number of similar crystals for the purpose of soaking experiments.

Therefore, crystals prepared in VDX plates with 19–21%(*w*/*v*) PEG 3000, 0.1 *M* buffer system II pH 5.0, 0.2 *M* zinc acetate were used for soaking experiments with maltooligosaccharides (purchased from Sigma–Aldrich and Megazyme). Initial soaks were carried out by adding maltooligosaccharide stocks directly into the crystallization drops in a 1:1 volume ratio. Crystals were soaked over various time spans (from 15 min to one week) in final concentrations of either 0.1 *M* maltoheptaose, 0.1 *M* maltopentaose or 0.5 *M* maltose. Another approach was also taken in which crystals [grown in 20%(*w*/*v*) PEG 3000, 0.1 *M* buffer system II pH 5.0, 0.2 *M* zinc acetate] were transferred to a 2.0 µl drop consisting of solely 25%(*w*/*v*) PEG 3000 and 0.5 *M* maltose. This was performed

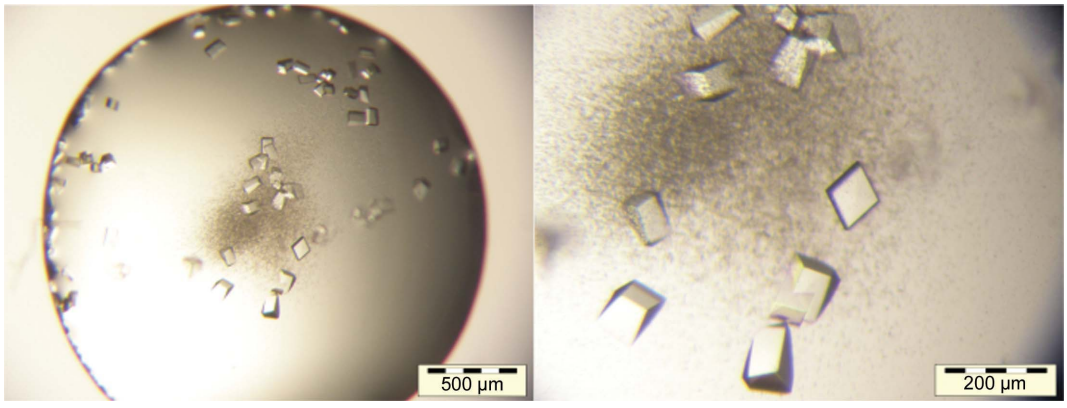

Figure 1
Crystals of Zn-*Ao*AA13. These crystals were obtained in VDX plates using 20%(*w*/*v*) PEG 3000, 0.2 *M* zinc acetate, 0.1 *M* buffer system II pH 5.0.

Table 2
Structure refinement and validation statistics.

Values in parentheses are for the outer shell.

	Zn-*Ao*AA13 (unliganded)	*Ao*AA13-His91flip	*Ao*AA13-G2(α1,4)	*Ao*AA13-G3(α1,4)G1(α1,6)
Resolution range (Å)	30.00–1.65 (1.69–1.65)	30.00–1.30 (1.33–1.30)	30.00–1.10 (1.13–1.10)	40.00–1.60 (1.64–1.60)
Completeness (%)	98.72 (87.57)	98.1 (87.5)	99.9 (99.6)	99.4 (93.1)
No. of reflections, working set	25174 (1612)	45856 (2971)	76110 (5575)	25429 (1822)
No. of reflections, test set	900 (57)	1627 (113)	2677 (196)	906 (65)
Final R_{cryst} (%)	12.40	9.16	10.08	11.25
Final R_{free} (%)	19.88	13.52	12.45	17.82
Cruickshank DPI	0.1198	0.0395	0.0243	0.0825
No. of non-H atoms				
Protein	1896	2032	2088	1862
Ion	9	4	12	4
Ligand	—	—	23	45
Water	327	436	384	293
Total	2232	2472	2507	2204
R.m.s. deviations				
Bonds (Å)	0.0179	0.0191	0.023	0.018
Angles (°)	1.7140	1.9885	2.038	1.678
Average *B* factors (Å^2)				
Protein†	15.580	8.643	7.361	11.711
Ion	23.612	13.696	10.065	13.975
Ligand	—	—	11.307	29.376
Water	25.639	24.733	25.485	23.609
Ramachandran plot‡				
Most favoured (%)	88.9	90.9	91.9	91.4
Allowed (%)	11.1	9.1	8.1	8.6

† Glycosylation (a single *N*-acetylglucosamine unit) and the active-site metal are included in 'Protein'. ‡ Calculated using *PROCHECK* in the *CCP*4 suite.

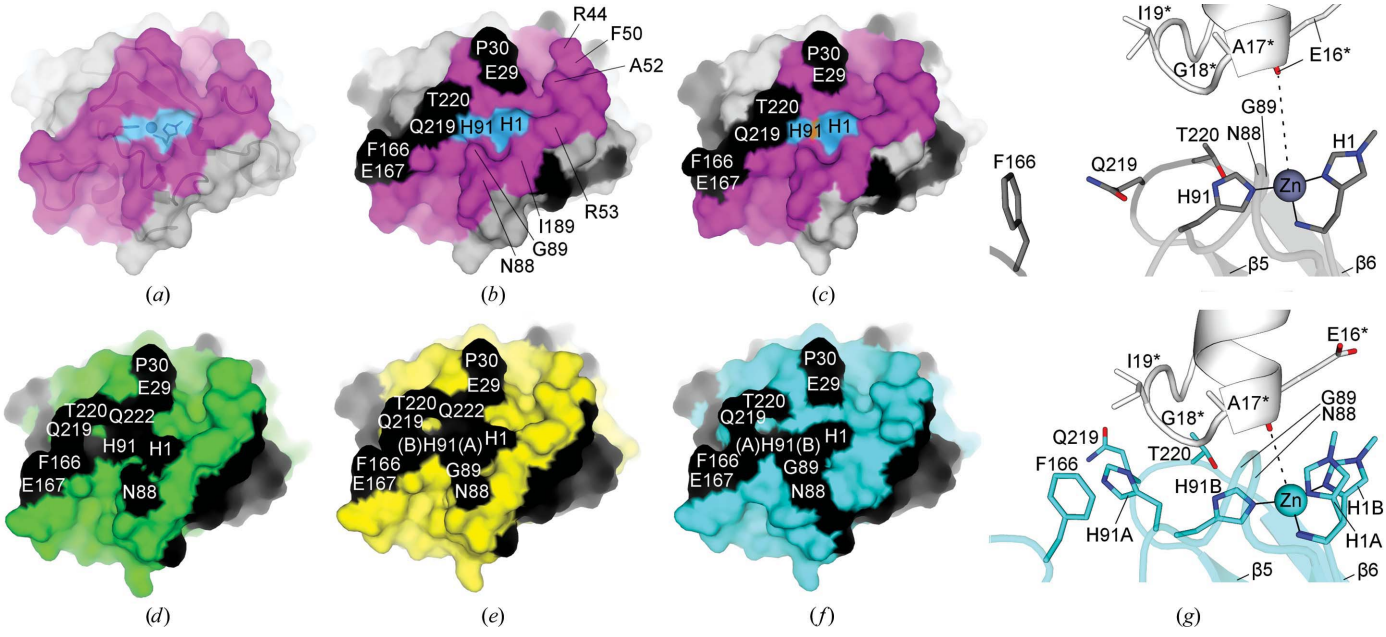

Figure 2
Substrate-binding groove in *Ao*AA13 structures. Surfaces of residues involved in crystal contacts are coloured black in (*b*)–(*f*). (*a*, *b*) The Zn-*Ao*AA13 structure (grey surface) with the proposed substrate-binding groove (residues 1, 25–31, 42–45, 49–55, 85–92, 166–176, 178–180, 189, 193 and 219–224) coloured magenta. The His brace (H1 and H91) is indicated in light blue. (*c*) The Cu-*Ao*AA13 structure coloured similarly to Zn-*Ao*AA13. The active-site copper is indicated by a copper-coloured surface. (*d*, *e*, *f*) In *Ao*AA13-G2(α1,4) (green), *Ao*AA13-G3(α1,4)G1(α1,6) (yellow) and *Ao*AA13-His91flip (cyan), local changes in the crystal packing cause additional residues of the substrate-binding groove (including the His brace) to be involved in crystal contacts. (*g*) The crystal contacts near the active site. Top: in Cu-*Ao*AA13 or zinc-containing conditions (exemplified by Zn-*Ao*AA13) the His brace is relatively accessible. Distances between the symmetry-related Glu16* backbone amide O and active-site metal (black dashes) are 6.3 and 6.4 Å for Zn-*Ao*AA13 and Cu-*Ao*AA13, respectively. Bottom: after transfer into conditions devoid of Zn (exemplified here by *Ao*AA13-His91flip) the Glu16*–Zn distance (black dashes) is shortened (3.9–4.1 Å), thus limiting access to the groove and active site. For residues in (*g*) with alternative conformations (except for the His brace) only the highest occupied conformation is shown.

to heavily dilute the zinc concentration, as the zinc ions present in the crystallization condition were speculated to impair substrate binding (see §3). The same method was used with longer maltooligosaccharides, transferring the crystals to a 2.0 µl drop consisting of solely 25%(*w*/*v*) PEG 3000 and 50 m*M* maltopentaose or 50 m*M* maltoheptaose. Under these conditions, the crystals soaked with the longer maltooligosaccharide had a tendency to fragment; to prevent this, protein at low concentration was included in the drop for soaking. Introducing 1 mg ml^{-1} protein into the soaking solution (still without the zinc) made the crystals much more amenable to the soaking experiment, avoiding the problems of cracking (although perhaps also competing for oligosaccharide binding). For soaks with branched substrates, such as 6^3-α-D-glucosyl-maltotriose (glucosyl-maltotriose) and 6^3-α-D-glucosyl-maltotriosyl-maltotriose, crystals were also moved to drops consisting of 25%(*w*/*v*) PEG 3000, 1 mg ml^{-1} *Ao*AA13 protein and either 130 m*M* 6^3-α-D-glucosyl-maltotriosyl-maltotriose or 125 m*M* glucosyl-maltotriose and then soaked for 2 and 18 h, respectively, before being mounted (Supplementary Fig. S1*d*).

Cocrystallization screening was also performed in which 20 m*M* maltopentaose was mixed (in an approximate equimolar ratio) with *Ao*AA13 (4 mg ml^{-1}) and incubated for 1 h. The chosen conditions were optimized in both MRC and VDX plates, varying both the protein and precipitant concentration. Crystals suitable for mounting and data collection only grew from the same condition as for the ligand-free enzyme [namely 20%(*w*/*v*) PEG 3000, 0.2 *M* zinc acetate, 0.1 *M* imidazole pH 8.0] and were isomorphous to the previous crystals. Diffraction data were collected to 1.1 Å resolution on MX beamline I911-3 at MAX-lab, but no bound maltopentaose was found when inspecting the electron density (not shown).

2.3. Data collection and processing

The data sets described here were collected on beamline I911-3 at MAX-lab, Lund, Sweden or on beamline ID14-4 at ESRF, Grenoble, France, and were processed and scaled using *XDS* and *XSCALE* (Kabsch, 2010) in space group $P2_12_12_1$, with unit-cell parameters similar to those of Cu-*Ao*AA13 (Lo Leggio *et al.*, 2015). Several data sets were

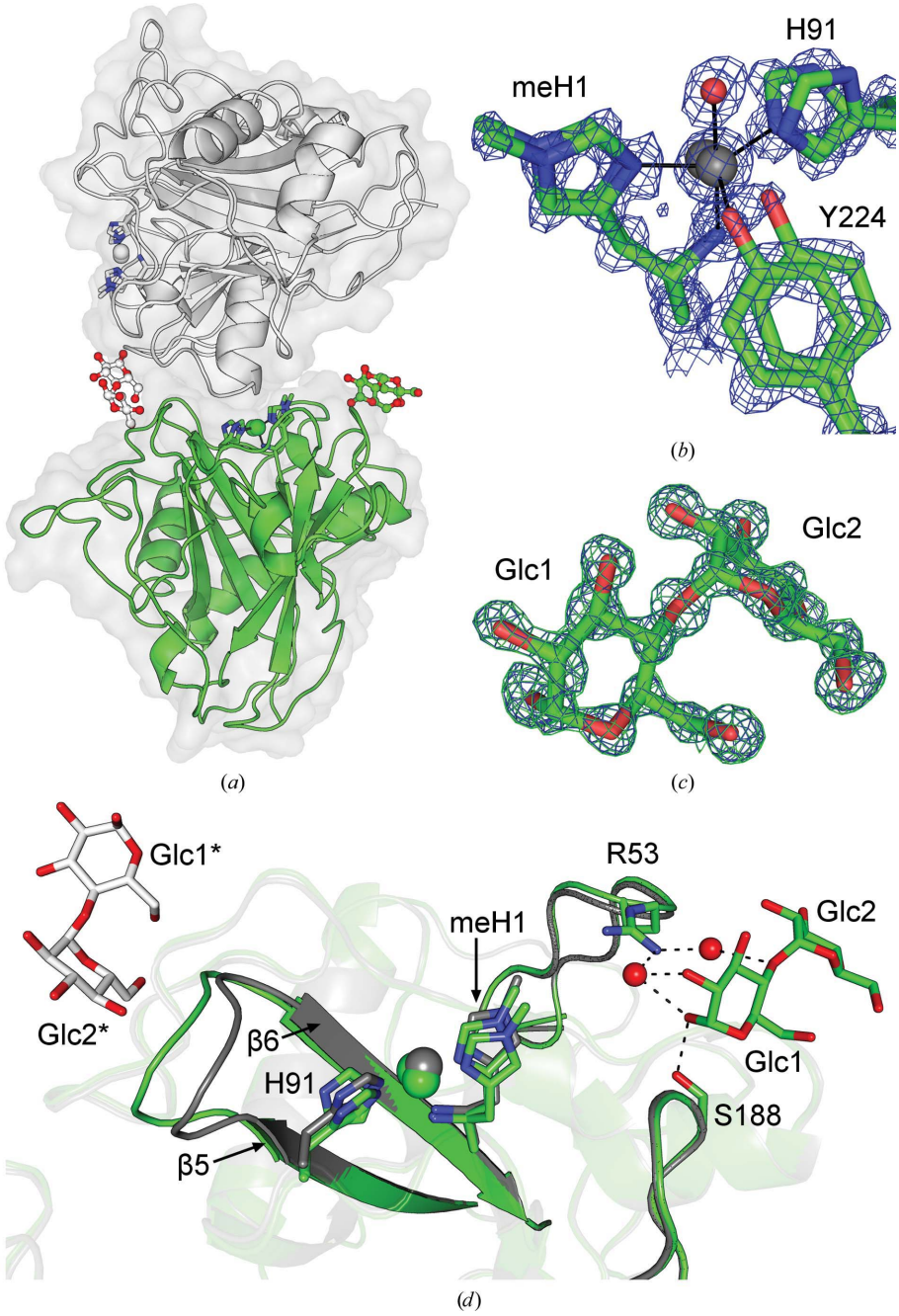

Figure 3
Structure of *Ao*AA13-G2(α1,4). (*a*) The *Ao*AA13-G2(α1,4) structure (green) interacting with maltose along with a symmetry-related molecule (white) involved in crystal contacts near the active site. (*b*) Disorder of the *Ao*AA13-G2(α1,4) metal-binding site with the metal-binding residues in two conformations and the $2F_o - F_c$ map in blue. (*c*) Electron density for the maltose ligand [$2F_o - F_c$ map (blue) and $F_o - F_c$ map (green)] calculated prior to incorporation of the ligand. In both (*b*) and (*c*) the $2F_o - F_c$ and $F_o - F_c$ maps are contoured at 1σ and 3σ, respectively. (*d*) Principal protein–ligand interactions in *Ao*AA13-G2(α1,4) and the position of maltose relative to the His brace. Direct and water-mediated interactions (red spheres) with Arg53 and Ser188 (green sticks) are shown. A symmetry-related maltose molecule (white) interacting with the β5–β6 loop is also shown. Zn-*Ao*AA13 is shown for comparison (grey).

collected, a selection of which are presented here. A data set was collected to 1.65 Å resolution from a crystal that was not soaked with ligand but was grown in the presence of zinc (hereafter referred to as Zn-*Ao*AA13). A crystal soaked (3 h) in solely 25%(*v*/*v*) PEG 3000 and 0.5 *M* maltose diffracted to 1.10 Å resolution [hereafter denoted *Ao*AA13-G2(α1,4)], while a crystal soaked for 18 h in 25%(*v*/*v*) PEG 3000, 125 m*M* glucosyl-maltotriose and 1 mg ml^{-1} *Ao*AA13 diffracted to 1.60 Å resolution [hereafter denoted *Ao*AA13-G3(α1,4)G1(α1,6)]. Finally, a structure was obtained to 1.30 Å resolution (*Ao*AA13-His91flip) from a crystal soaked with maltopentaose for 48 h but where further analysis (see below) showed no maltopentaose density. Data statistics are summarized in Table 1.

2.4. Structure solution and refinement

One round (20 cycles) of rigid-body refinement was run in *REFMAC*5 (Murshudov *et al.*, 2011) from the *CCP*4 suite (Collaborative Computational Project, Number 4, 1994; Winn *et al.*, 2011) using the previously solved structure of Cu-*Ao*AA13 (PDB entry 4opb; Lo Leggio *et al.*, 2015) stripped of water and other solvent molecules as the model. R_{free} flags were also imported from the previous structure-factor file and extended to a higher resolution limit when appropriate. The preliminary structures were refined by multiple rounds of restrained refinement. The structures of both *Ao*AA13-G2(α1,4) and *Ao*AA13-His91flip were refined anisotropically, while those of *Ao*AA13-G3(α1,4)G1(α1,6) and Zn-*Ao*AA13 were refined isotropically for all water molecules and anisotropically for all other atoms (protein, metal ions, glycosylation).

2.5. Structure analysis

Structures (and ligands) were modelled, inspected and validated (*e.g.* using Ramachandran plot, geometry and rotamer analysis) in *Coot* (Emsley & Cowtan, 2004; Emsley *et al.*, 2010; Debreczeni & Emsley, 2012). Zinc-ion occupancies were modelled based on their correlations with difference map and anomalous Fourier map density, as well as with appropriate *B* factors. *PROCHECK* (Morris *et al.*, 1992; Laskowski *et al.*, 1993), *SFCHECK* (Vaguine *et al.*, 1999), *BAVERAGE* and *CONTACT* (*CCP*4 suite) were also used for final structure validation and for crystal contact analysis (looking for intermolecular contacts of ≤4 Å). Refinement and validation statistics are summarized in Table 2

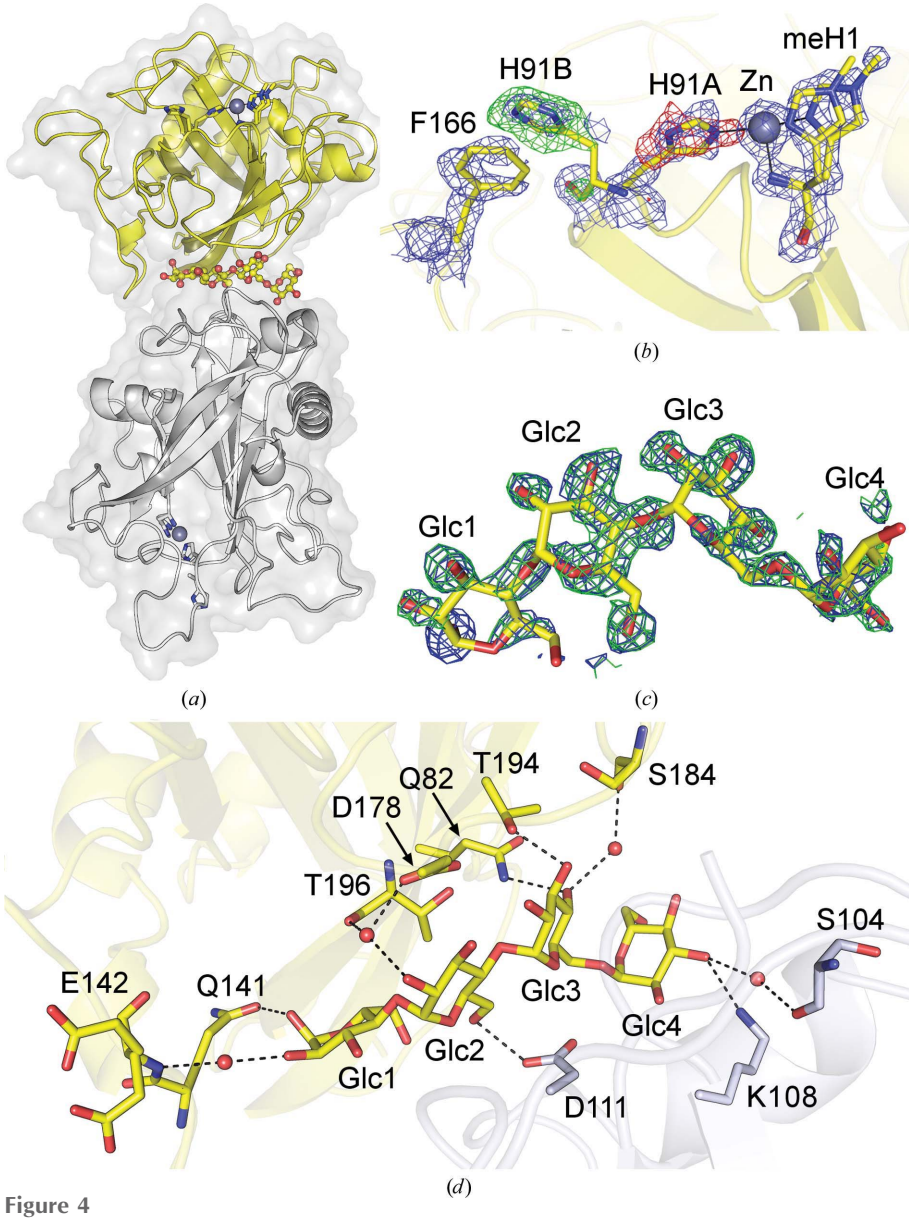

Figure 4
The *Ao*AA13-G3(α1,4)G1(α1,6) structure. (*a*) The *Ao*AA13-G3(α1,4)G1(α1,6) structure (yellow) and a symmetry-related molecule (white) with the His brace (coloured according to molecule) shown as sticks. The active-site Zn is shown as a sphere (grey). The glucosyl-maltotriose ligand is bound in between the two molecules. (*b*) The His brace is shown in a native conformation (70% occupancy) and in an alternative conformation (30% occupancy) as modelled in the final structure. The maps shown are $2F_o - F_c$ (blue) and $F_o - F_c$ (green for positive and red for negative) difference maps from a model with fully occupied His91A only, and are contoured at 1.0σ and ±3.0σ, respectively. As shown, modelling a fully occupied native conformation leads to negative difference map density near the active-site metal and positive difference map density near Phe166. (*c*) Electron density for glucosyl-maltotriose calculated prior to incorporation of the ligand. The $2F_o - F_c$ (blue) and $F_o - F_c$ (green) maps are shown at contour levels of 0.7σ and 2.5σ, respectively. (*d*) Glucosyl-maltotriose interactions with *Ao*AA13 (yellow) and a symmetry-related molecule (white). Principal direct interactions are formed through Gln82, Gln141 and Thr194 to Glc1 and Glc3.

3. Results

3.1. Overview of *Ao*AA13 structures

Expressed and purified *Ao*AA13 was crystallized and some crystals were soaked with maltooligosaccharides. From an unsoaked crystal, the unliganded zinc-bound structure (Zn-*Ao*AA13) was refined. The structure reveals an active site with two clearly defined water ligands in the open equatorial and axial positions with distances of 2.3 and 2.4 Å, respectively. The His brace [formed by the methylated His1 (meHis1) and His91] coordinates the zinc in the other equatorial positions with distances of 2.0–2.2 Å, while the distance to Tyr224 in the axial position is 2.4 Å (Supplementary Fig. S2*a*). All active-site residues are well defined and modelled in a single conformation. The active site of *Ao*AA13 sits in a shallow groove (Fig. 2) previously suggested to be involved in substrate interactions (defined as residues 1, 25–31, 42–45, 49–55, 85–92, 166–176, 178–180, 189, 193 and 219–224 in Lo Leggio *et al.*, 2015). Although a number of alcohol ligands (often carbohydrate mimics) were found in the groove of the original Cu-*Ao*AA13 structure (PDB entry 4opb), the role of the groove in substrate interaction still needed to be experimentally confirmed.

The Zn-*Ao*AA13 structure (as well as that of Cu-*Ao*AA13) shows that the area near the active site is involved in crystal contacts. Analysing the interfaces of Zn-*Ao*AA13 using *PISA* reveals three significant interfaces of >150 Å^2, of which one is involved in crystal contacts only at the border of the groove [the residues involved in crystal contacts in Zn-*Ao*AA13 (Glu29, Pro30, Phe166, Glu167, Gln219 and Thr220) are similar to those in Cu-*Ao*AA13 ;Fig. 2]. Thus, the groove and active site were relatively accessible, providing the rationale for soaking experiments (cocrystallization experiments with maltopentaose did not result in structures with bound ligands; see §2).

Data collected from crystals in the initial soaking experiments (not shown) showed no difference density in the initial electron-density maps that could account for maltooligosaccharides. One cause of concern was that the high concentration of zinc ions in the crystallization condition prevented binding, since many ions were seen to be bound to the surface of the protein in the Zn-*Ao*AA13 structure, in contrast to the Cu-*Ao*AA13 structure obtained using a different, but not very reproducible, crystallization procedure (see §2 for details).

Thus, soaking with a solution depleted of zinc ions was performed. This proved to be successful when soaking with maltose, since *Ao*AA13-G2(α1,4) clearly showed the presence of very well defined electron density for maltose between two symmetry-related molecules, which could be modelled with 90% occupancy (Figs. 3*a* and 3*c*). In general, structures obtained from crystals soaked in conditions devoid of zinc contained fewer Zn atoms in the structure (Supplementary Table S2).

With this result in mind, it was obvious to try to use the new procedure for soaking to achieve complexes with longer and branched maltooligosaccharides. Unfortunately, soaking experiments with maltopentaose and maltoheptaose resulted

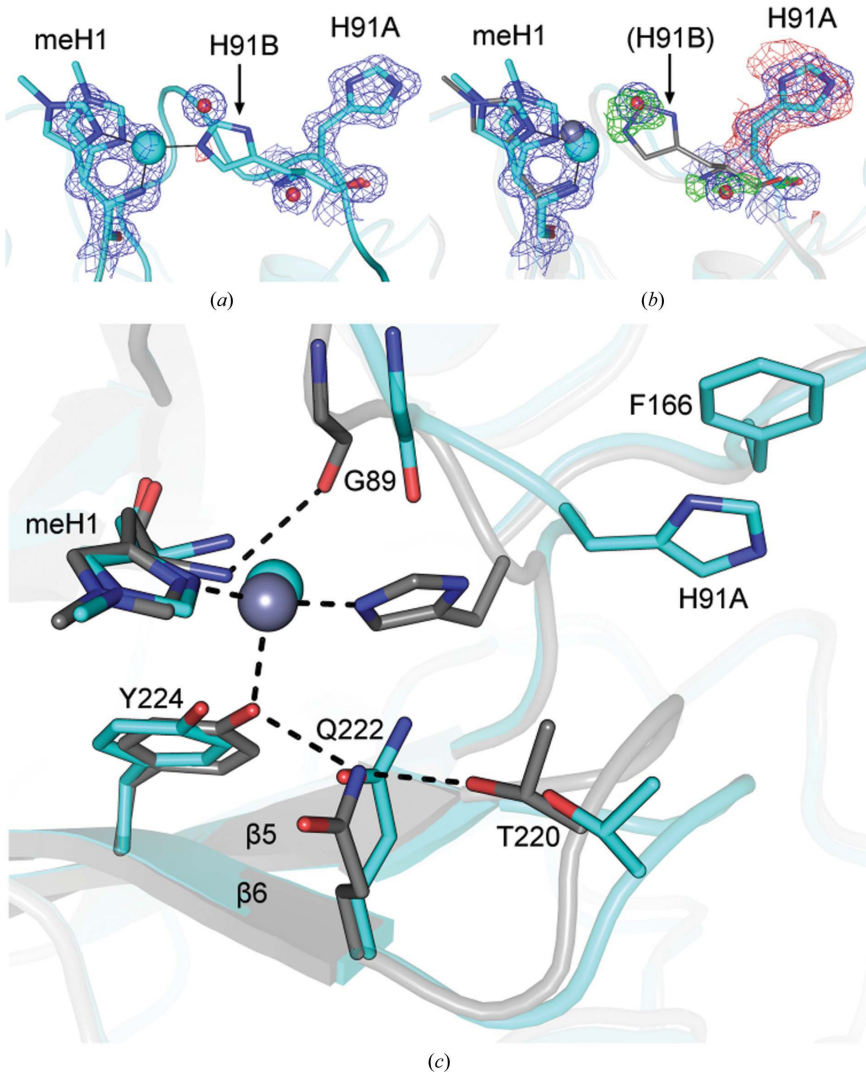

Figure 5
Active site of *Ao*AA13-His91flip. (*a*) The protein is shown in cyan with the His brace as sticks. The active-site residue His91 is modelled in a native (H91B) and non-native (H91A) conformation with 20 and 80% occupancy, respectively. (*b*) The $2F_o - F_c$ (blue, at 1.0σ) and $F_o - F_c$ (green, at 2.0σ) maps shown as calculated for the fully occupied flipped conformation of His91 (100% occupancy of H91A). The fully ordered active site of Zn-*Ao*AA13 (grey) is shown for comparison. (*c*) The active site of *Ao*AA13-His91flip (the Thr220–Gln222–Tyr224 and Gly89–meHis1 interactions are lost) compared with Zn-*Ao*AA13. The β5–β6 loop moves away from the active site. His91 flips out of the active site (H91A), interacting with Phe166. The vacant position of H91A is partly occupied by Gln222 and Gly89, which lose interactions with the active-site residues meHis1 and Tyr224.

Table 3
*Ao*AA13 interactions with maltose.

	*Ao*AA13-G2(α1,4)				
	Glycosidic atom	Residues (bck/sc†)	Protein atom‡	Distance (Å)	Interaction type
Glc1 (α1,4)	O1	Ser188(sc)	O^{γ}	2.7	Direct
	O1	Arg53(sc)	N^{η}	3.4	Direct
	O1	Arg53(sc)	H_2O (N^{η})	2.9	Mediated
	O2	Arg53(sc)	H_2O (N^{η})	2.6	Mediated
	O4	Arg53(sc)/Ser21(sc)	H_2O (N^{η}/O^{γ})	3.1	Mediated
	O5	Ser188 (bck)	O	3.3	Direct
	O5	Ser188(bck)	H_2O (O)	3.1	Mediated
	O6	Ser18(bck)	H_2O (O)	2.8	Mediated
Glc2 (α1,4)	O2	Arg53(sc)/Ser21(sc)	H_2O (N^{η}/O^{γ})	3.1	Mediated
	O3	Asp54(sc)/Asn219(bck)§	H_2O (O^{δ}/O)	2.7	Mediated
	O4	Phe218(bck)§	O	2.7	Direct
	O5	Ser32(sc)§	H_2O (O^{γ})	2.8	Mediated
	O6	Ser32(sc)§	H_2O (O^{γ})	3.2	Mediated
	O6	Ser33(bck)§	N	3.1	Direct

† Backbone (bck)/side chain (sc). ‡ For water-mediated protein–ligand interactions the protein atom interacting with the water molecule is given in parentheses. § Symmetry-related.

Table 4
*Ao*AA13 interaction with glucosyl-maltotriose.

	*Ao*AA13-G3(α1,4)G1(α1,6)				
	Glycosidic atom	Residues (bck/sc†)	Protein atom‡	Distance (Å)	Interaction type
Glc1 (α1,4)	O1	Gln141(sc)	O^{ε}	2.5	Direct
	O2	Glu142(bck)	H_2O (N)	2.5	Mediated
	O4	Thr196(bck)/Asp178(sc)	H_2O (O/O^{δ})	3.0	Mediated
Glc2 (α1,4)	O2	Thr196(bck)/Asp178(sc)	H_2O (O/O^{δ})	2.8	Mediated
	O6	Asp111(sc)§	O^{ε}	2.9	Direct
Glc3 (α1,4)	O3	Thr194(sc)	O^{γ}	2.7	Direct
	O4	Gln82(sc)	N^{ε}	2.9	Direct
	O4	Ser184(bck)	H_2O (O)	2.7	Mediated
Glc4 (α1,6)	O2	Asp111(sc)§	O^{δ}	2.4	Mediated
	O3	Lys108(sc)§	N^{ζ}	3.0	Direct
	O3	Ser104(bck)§	H_2O (O)	2.8	Mediated

† Backbone (bck)/side chain (sc). ‡ For water-mediated protein–ligand interactions the protein atom interacting with the water molecule is given in parentheses. § Symmetry-related.

in neither of the ligands being bound in the structures. For branched oligosaccharides the method was to some extent successful when soaking with glucosyl-maltotriose as, in unbiased $2F_o - F_c$ and $F_o - F_c$ maps at 0.7σ and 2.5σ, respectively, the density was relatively well defined for the maltotriose portion (Fig. 4*c*). In the final refined structure of *Ao*AA13-G3(α1,4)G1(α1,6) the glucosyl-maltotriose ligand was modelled with 70% occupancy.

For the data sets collected from soaked crystals, oligosaccharide ligands were found only in two structures, namely *Ao*AA13-G2(α1,4), further described in §3.2, and *Ao*AA13-G3(α1,4)G1(α1,6), further described in §3.3. In these structures some disorder of the His brace and other residues near the active site is observed, as will be described in more detail below. For one of the crystals soaked with maltopentaose, although no obvious oligosaccharide binding occurred, the observed disorder is extreme. The principal conformation of His91 (80% occupancy) was flipped away from meHis1, resulting in a completely misfolded active site (Fig. 5*a*). The structure was named *Ao*AA13-His91flip based on this observation, and is further described in §3.4.

The three structures obtained with crystals from zinc-depleted soaking conditions show local changes in the crystal packing (Fig. 2*g*) compared with the Zn-*Ao*AA13 and Cu-*Ao*AA13 structures. These changes were not observed for crystals from the same tray soaked with maltose in the presence of Zn for even as long as a week, so the changes are not attributable to the presence of oligosaccharides alone. In *Ao*AA13-G2(α1,4), *Ao*AA13-G3(α1,4)G1(α1,6) and *Ao*AA13-His91flip the molecular interfaces reported by *PISA* were somewhat larger than for Zn-*Ao*AA13 (and Cu-*Ao*AA13), and additional groove residues in the vicinity of the active site, as well as the His brace itself (His1, Asn88, Gly89, His91 and Gln222 in Fig. 2), were reported to be involved in crystal contacts, despite the similar unit-cell parameters. Although this new packing limits the access to the active site, large parts of the proposed substrate-binding groove still appeared to be largely accessible (*e.g.* in between Glu29, Pro30, Arg44, Phe50 and Ala52 in Fig. 2). Surprisingly, though, bound ligands were only found outside the proposed substrate-binding groove.

3.2. Binding of the maltose ligand

In *Ao*AA13-G2(α1,4) maltose is found between two symmetry-related molecules (Fig. 3 and Table 3). Analysis with *PISA* reveals that one molecule has a slightly higher surface interface with maltose. Assigning maltose to the molecule with the greater interaction interface places it somewhat within reach of the active site (Fig. 3).

Two amino acids are potentially within hydrogen-bonding distance of the maltose moiety, namely Arg53 and Ser188 (Fig. 3). In *Ao*AA13-G2(α1,4) Arg53 is less well defined than in the native structure (Cu-*Ao*AA13), and although the $F_o - F_c$ density did suggest that Arg53 also exists in a partial conformation within hydrogen-bonding distance of the maltose ligand, the residue was modelled in one conformation similar to that of Cu-*Ao*AA13. The Arg53 side chain comes within a distance of 3.4 Å of the C1 hydroxyl from the glucosyl unit from the reducing end (hereafter denoted Glc1). The Arg53 residue is involved in water-mediated hydrogen bonds to both Glc1 O1 and Glc1 O2. Additional hydrogen bonds are gained through another water molecule from Glc1 O4 (the glycosidic linkage) and Glc2 O2 to both Arg53 and Ser21. Ser188 makes a 2.7 Å hydrogen bond to Glc1 O1 and a water-mediated hydrogen bond to Glc1 O6 (Fig. 3). Hydrogen bonds are also

made to Glc2 from the peptide backbone of a symmetry-related molecule (Fig. 3, white). The backbone amide N atom of Ser33* (residues from symmetry-related molecules are indicated with asterisks) contacts Glc2 O6, while Ser32* makes a water-mediated hydrogen bond (bidentate) to both Glc2 O6 and Glc2 O5. Lastly, the amide O atoms of Phe218* and Gln219* (in the loop connecting β5 and β6 in Fig. 3) make hydrogen bonds (direct and water-mediated) to Glc2 O4 and Glc2 O3, respectively. All interactions are summarized in Table 3.

Some disorder of the active-site residues is observed in this structure (a main and an alternate conformation were modelled with 80 and 20% occupancy, respectively, for each of meHis1, His91, Gln222 and Tyr224), although all alternate conformations are close in space to the main conformation. Since the maltose complex is one of the highest resolution LPMO structures to date, and this would be mechanistically interesting [especially in the light of an observed hydrogen-bonding network in the active site of the *Ls*AA9A complex structures (Frandsen *et al.*, 2016) and the proposed tautomerization of the terminal amine of meHis1 during catalysis (Gagnon & Tolman, 2015; Walton & Davies, 2016; Dhar & Tolman, 2015)], we checked to see whether hydrogen could be clearly identified in a difference map. Indeed, many H atoms are clearly visible in well ordered regions (Supplementary Figs. S2*b* and S2*c*), but unfortunately this is not the case at the active site owing to the observed disorder.

3.3. Binding of the glucosyl-maltotriose ligand

The *Ao*AA13-G3(α1,4)G1(α1,6) structure showed the bound glucosyl-maltotriose ligand interacting with two molecules but quite far from the active site of both (Fig. 4*a* and 4*c*). Analysis with *PISA* reveals that one molecule has a greater surface interface with the maltotriose part of the ligand. The same molecule also makes the most polar interactions with the ligand (Table 4). Only the α-1,6-linked glucose branch (Glc4) has a greater interface with a symmetry-related molecule (Fig. 4*d*). Based on this, the glucosyl-maltotriose was assigned to the molecule with the most interactions. The only three amino-acid residues that come within reach of hydrogen-bonding distance (3.2 Å) are Gln82, Gln141 and Thr194 (Fig. 4). The first glucose residue (from the reducing end; hereafter denoted Glc1) of the ligand interacts *via* the C1 hydroxyl (Glc O1) with Gln141 through a 2.5 Å hydrogen bond. An additional interaction is gained from a water-mediated hydrogen bond to the backbone amide of Glu142. Both Glc1 O4 (glycosidic bond) and Glc2 O2 make water-mediated bidentate hydrogen bonds to Asp178 O^{δ} and the backbone amide of Thr196. Glc2 O6 comes within reach (distance 2.9 Å) of Asp111* O^{δ} from a symmetry-related molecule, although the geometry is slightly unfavourable for a hydrogen bond (C6—O6—Asp111* O^{δ} angle of 80°). An additional 2.9 Å contact to the same symmetry-related molecule exists between Glc2 O5 and Pro112* C^{δ} (which seems unfavourable). Glc3 O3 makes the strongest interaction (distance of 2.7 Å) to Thr194 O^{γ}, while Glc3 O4 makes a hydrogen bond with a distance of 2.9 Å to Gln82 N^{ε}. It also makes an additional water-mediated hydrogen bond (2.7 Å) to the carbonyl of Ser184. Glc4, the least well defined residue, makes hydrogen bonds (two water-mediated and one direct with Lys108*) to a symmetry-related molecule. All interactions are summarized in Table 4.

There is also a disordered active site in the *Ao*AA13-G3(α1,4)G1(α1,6) structure. However, unlike in *Ao*AA13-G2(α1,4), where all alternate conformations of the active-site residues are close to the main conformations, here His91 had to be partly modelled in a conformation flipped away from the active site (H91B, with 30% occupancy, in Fig. 4*b*; His91A N^{ε}—His91A/B C^{α}—His91B N^{ε} angle of ∼115°) where it does not interact with the active-site metal ion.

3.4. *Ao*AA13-His91flip structure

As described above, in the Zn-*Ao*AA13 structure the active-site residues (meHis1, His91 and Tyr224) are fully ordered, while in the complex structures obtained from soaking in zinc-depleted conditions, *Ao*AA13-G2(α1,4) and *Ao*AA13-G3(α1,4)G1(α1,6), some disorder of active-site residues is observed.

The *Ao*AA13-His91flip structure presents an extreme case of active-site disorder, where the main conformation of His91, with 80% occupancy (H91A in Fig. 5), is flipped ∼120° relative to the native conformation in which it can bind the active-site metal. There is, however, evidence for a 20% occupancy of the native metal-binding conformation, since modelling a fully occupied flipped conformation of His91 leads to negative density in the $F_o - F_c$ map, while positive density appears near the active-site metal (Fig. 5*b*).

Other differences can be seen compared with the Zn-*Ao*AA13 structure. In the Zn-*Ao*AA13 structure Gln222 and Gly89 interact with Tyr224 and meHis1, respectively (Fig. 5*c*). In *Ao*AA13-His91flip, His91A makes favourable π–π stacking interactions with Phe166 (Fig. 5*c*). At the active site the Thr220–Gln222–Tyr224 and the Gly89–meHis1 interactions are lost, and Gln222 and Gly89 move towards the metal site, filling the empty space left by the movement of His91A (Fig. 5*c*). The β5–β6 loop (harbouring Thr220) moves away from the active site compared with Zn-*Ao*AA13. Effectively, the active site is severely misfolded compared with a metal-binding conformation.

4. Discussion

4.1. Biological relevance of oligosaccharide-bound structures

In the *Ao*AA13 structures presented here, none of the maltooligosaccharides interact directly with the active site (Fig. 6). A possible reason is that the local changes in crystal contacts occurring in structures from zinc-depleted conditions further limit access to the active site (Fig. 2).

The biological significance of the liganded structures is uncertain. Although a maltose residue comes within close distance of meHis1 in one complex (Fig. 3), the structures obtained here obviously do not mimic Michaelis–Menten complexes. This is in contrast to the *Ls*AA9A complex

structures (PDB entries 5acf, 5aci and 5acj), where the scissile glycosidic bond is positioned in the active site with the glucosyl unit in subsite +1 stacking with meHis1. When superimposing the *Ls*AA9A complex structures onto *Ao*AA13 it is clear that structural features in *Ao*AA13 (*e.g.* the side chain of Ile189; Fig. 2) interfere with the β-linked substrates in subsite +2. However, since AA13s act on α-linked glycosidic linkages, it is possible that *Ao*AA13 could accommodate α-linked substrates making stacking interactions with meHis1.

The maltose ligand in the *Ao*AA13-G2(α1,4) structure has the reducing-end C1 hydroxyl (Glc1 O1) pointing towards the protein molecule, but it is possible that a slightly altered mode of binding would allow an α-1,4-linked substrate to extend towards the active site. Thus, the maltose ligand in *Ao*AA13-G2(α1,4) could resemble binding in distant subsites (Fig. 6). In this regard it must be noted that the direction of the substrate (in terms of the reducing/nonreducing ends) would be the opposite of that in the *Ls*AA9A complex structures. In the light of the reported amylopectin activity (Vu *et al.*, 2014), it is also possible that extending the substrate through an α-1,6 linkage from Glc1 O6 of the maltose ligand could lead to the active site (Fig. 6), and thus the ligand could mimic interaction with a branched substrate such as amylopectin. The residues Arg53 and Ser188 (which interact directly with the maltose ligand) are almost completely conserved among AA13 members (Arg and Ser/Thr; Supplementary Fig. S3), supporting the relevance of this binding site. However, all of these suggestions remain highly speculative until further experimental evidence is acquired.

In the case of *Ao*AA13-G3(α1,4)G1(α1,6) the ligand is found quite far from the active site (Figs. 4*a* and 6). Interactions far from the active site were also found for *Nc*AA9C (PDB entry 4d7u), where substrate titrations (with xyloglucan polysaccharides) were monitored using NMR (Courtade *et al.*, 2016). Some of these interactions appear to be in similar positions as the interactions with glucosyl-maltotriose found in *Ao*AA13-G3(α1,4)G1(α1,6). Recently, secondary binding sites (termed surface binding sites; SBSs) have been recognized in several GH families, for example GH13 and GH77 (Cockburn *et al.*, 2014; Cuyvers *et al.*, 2012). These are sites distant from the active site which have an indirect positive effect on the turnover of the substrate through a variety of functions, such as substrate targeting, enhancing processivity and allosteric effects (Cockburn *et al.*, 2014; Cuyvers *et al.*, 2012). A common architecture of SBSs usually involves two aromatic residues positioned parallel to the enzyme surface with an angle of about 130° between them. The concave curvature is proposed to assist by accompanying the helical starch structures, and the motif is also shared with several starch-binding modules (Cuyvers *et al.*, 2012). The *Ao*AA13-G3(α1,4)G1(α1,6) structure could represent a similar secondary binding site for either branched or nonbranched substrates. The highly conserved Gln82, Gln141 and Thr194 (Supplementary Fig. S3) in AA13 members support the relevance of this proposed site, although the absence of aromatics is atypical for SBSs. It must be noted that LPMOs in general have very atypical substrate-binding surfaces compared with other carbohydrate-active enzymes. There is, for example, a general paucity of Trp residues on the surfaces of LPMOs.

No traces of maltose or maltopentaose were found at the G3(α1,4)G1(α1,6) binding site in any of the remaining structures. In *Ao*AA13-G3(α1,4)G1(α1,6) the most prominent protein interactions with the maltotriose part of the ligand are gained from Gln82, Gln141 and Thr194 to Glc1 and Glc3 (Fig. 4 and Table 4); therefore, it is possible that α-1,4-linked substrates with a DP of <3 will interact too weakly at this site. The C4 hydroxyl at the nonreducing end of the maltotriose part, Glc3 O4 (Fig. 6), is not obstructed, and thus there is sufficient space in the crystal for maltopentaose (or other α-1,4-linked substrates with a DP of >3) to bind. However, maltopentaose lacks the α-1,6-linked glucosyl unit which is also likely to aid binding, which may explain why maltopentaose did not bind.

Given the additional occlusion of the His brace in the crystals after rearrangement of the crystal packing in the described complexes, our results do not support, or disprove, the previously proposed AA13 binding site. Parts of the proposed substrate-binding groove were accessible, but no ligands were found here. Additional factors that could explain the lack of binding are that the oligosaccharides used in this

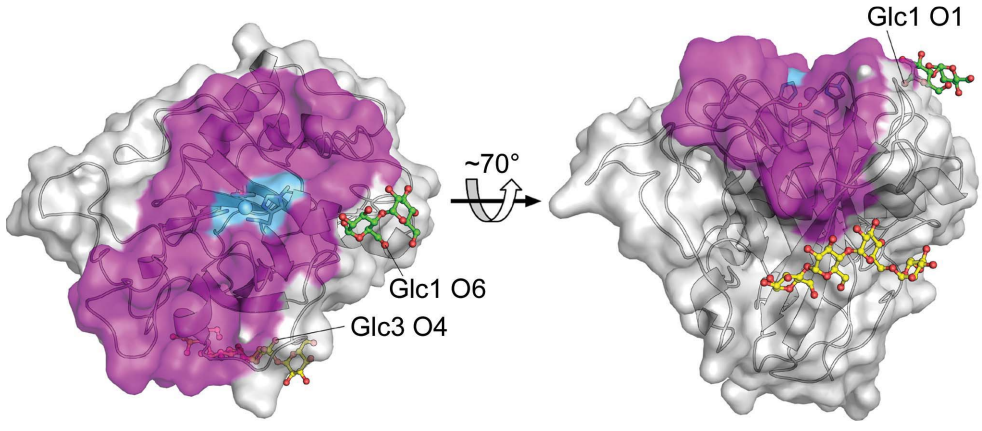

Figure 6
Maltooligosaccharide ligands bound in the *Ao*AA13 structures. The Zn-*Ao*AA13 structure is shown in grey, with the surface of the substrate-binding groove (residues 1, 25–31, 42–45, 49–55, 85–92, 166–176, 178–180, 189, 193 and 219–224) coloured magenta. The His brace and active-site zinc are shown as sticks and a sphere, respectively, and are indicated with a light blue surface. The maltose ligand of *Ao*AA13-G2(α1,4) (green) and the glucosyl-maltotriose ligand of *Ao*AA13-G3(α1,4)G1(α1,6) (yellow) are superimposed onto the Zn-*Ao*AA13 structure and shown in sticks to indicate their positions relative to each other and to the substrate-binding groove.

study are too poor mimics of the natural substrate, and that under the soaking conditions the active site is disordered (see §4.2). It is also possible that the conditions used here are inappropriate for ligand binding (note that the addition of NaCl and HCN enhanced substrate binding for *Ls*AA9A and *Nc*AA9C, respectively; Frandsen *et al.*, 2016; Courtade *et al.*, 2016). Considering all of the evidence, it is possible that the maltooligosaccharide-binding sites observed in the presented structures represent interactions with extended biologically relevant substrates (such as, for example, amylopectin or amylose), but given their position at symmetry contacts the ligands may also represent artefacts in the crystalline state.

4.2. Disordered active site

The disorder of the active site and movement of the $\beta5$–$\beta6$ loop (Figs. 5*c* and 3*d*) appear to correlate with an absence of active-site metal. Zinc is a good redox-inactive mimic of copper at LPMO active sites, and this was another reason why soaking in zinc-substituted *Ao*AA13 seemed attractive at the beginning of this project, since the enzyme would definitely be inactive and the disorder often observed in LPMO structures owing to the photoreduction of copper would be avoided. However, the His brace has lower affinity for zinc ions than for copper ions (Hemsworth *et al.*, 2013, 2014; Lo Leggio *et al.*, 2015; Quinlan *et al.*, 2011; Aachmann *et al.*, 2012), and it is clear that the zinc concentrations under the soaking conditions employed here were insufficient to maintain a fully occupied metal site.

In the uncomplexed structures Cu-*Ao*AA13 and Zn-*Ao*AA13 with a fully occupied active-site metal, the active-site residues are ordered and interact with the $\beta5$–$\beta6$ loop *via* hydrogen bonds between the backbone amides of His91 and Gln219 and between the side chains of Thr220, Gln222 and Tyr224 (Fig. 5*c*). In the absence of metal the active-site disorder interferes with these interactions and leads to movement of the $\beta5$–$\beta6$ loop (Figs. 3*d* and 5), which occurs for all of the three structures obtained under zinc-depleted conditions [*Ao*AA13-G2(α1,4), *Ao*AA13-G3(α1,4)G1(α1,6) and *Ao*AA13-His91flip]. Apparently, this allows the local changes in the crystal packing and additional crystal contacts (with meHis1, Asn88 and His91, and in some cases also Gly89 and Gln222) at the active site and proposed substrate groove (Fig. 2) [the crystal contacts with Gly89 are formed in the *Ao*AA13-G3(α1,4)G1(α1,6) and *Ao*AA13-His91flip structures following the rearrangement of His91; Fig. 5]. This explains the increased crystal lattice interface (reported by *PISA*) in these three structures.

Despite the relatively tight packing around His91 in the three structures from soaked crystals, Zn-*Ao*AA13 has fewer crystal contacts around the His brace (Fig. 2*g*), and it is conceivable that even more extreme flipping of His91 could occur *in situ*. However, it is also possible that the more drastic His91 rearrangement seen only in some structures is an effect related to the long storage of the apoprotein sample, since apart from Zn-*Ao*AA13 the structures presented here were obtained using a protein batch stored for some time in the absence of divalent metals. For other families of LPMOs it has been reported that copper binding increases protein stability (Gregory *et al.*, 2016; Johansen *et al.*, 2012). Copper was not included in in the storage buffer as this could lead to undesired Fenton chemistry if trace amounts of promiscuous electron donors were present. Indeed, for some families of LPMOs it has been shown that copper-loaded enzymes in the absence of substrate produce H_2O_2 (and potentially other protein-damaging reactive oxygen species; Kittl *et al.*, 2012; Isaksen *et al.*, 2014; Bennati-Granier *et al.*, 2015), which can lead to enzyme inactivation (Scott *et al.*, 2016).

The absence of an active-site metal has been reported to decrease the rigidity of the active-site residues in other LPMOs (Aachmann *et al.*, 2012; Vaaje-Kolstad *et al.*, 2005; Hemsworth *et al.*, 2013; Chiu *et al.*, 2015). Structures of AA10s from *Bacillus amyloliquefaciens* (*Ba*AA10A; Hemsworth *et al.*, 2013) and *Enterococcus faecalis* (*Ef*AA10A; Vaaje-Kolstad *et al.*, 2012; Gudmundsson *et al.*, 2014) have copper-bound active sites (PDB entries 2yoy and 2yox, and PDB entries 4alc and 4alt, respectively) which are very similar to those of Cu-*Ao*AA13 (and Zn-*Ao*AA13). However, the *Ba*AA10A and *Ef*AA10A apo structures (PDB entries 2yow and 4a02, respectively) show a repositioning of the internal active-site histidines (His125 in *Ba*AA10A and His114 in *Ef*AA10A). Interestingly, these histidines interact with residues (Asp191 in *Ba*AA10A and Asp180 in *Ef*AA10A) in a loop equivalent to the $\beta5$–$\beta6$ loop in *Ao*AA13. Furthermore, in a recent EPR study, heterogeneity of the active site of an AA10 is reported (Chaplin *et al.*, 2016). The authors report two distinct copper-bound forms that differ in the coordination of the amino group of the N-terminal His (*i.e.* three-coordinated and two-coordinated copper, respectively). The structure of an AA9 from *Thermoascus aurantiacus* (*Ta*AA9A; PDB entry 3zud) shows the active-site copper modelled in two (quite different) conformations, one of which has an N–metal distance of >4.0 Å (Quinlan *et al.*, 2011). Similarly, the *Ao*AA13-G2(α1,4) active-site metal (although zinc in this case) and His brace are also modelled in two conformations. It is, however, not clear whether the difference in N–metal distances (0.1 Å) of the two conformations in *Ao*AA13-G2(α1,4) is significant (as is the case for *Ta*AA9A, where it is 1.4 Å). From this it seems that the plastic nature of the AA13 active site described here is shared with members of other families and perhaps is a general feature of LPMOs.

5. Conclusion and perspectives

In this study, we set out to obtain substrate complexes with the zinc-substituted form of an AA13 family enzyme. The initial efforts were hampered by an excess of zinc ions in the putative substrate-binding groove. A strategy in which soaks were carried out in solutions depleted of zinc ions showed unexpected local rearrangements of crystal packing, which occlude the histidine brace. Furthermore, we observed active-site disorder, which in its most extreme case caused a severe rearrangement of the internal His of the His brace. The *Ao*AA13-His91flip structure provides a rare example of a

three-dimensional structure of a heavily misfolded enzyme active site, and highlights the important role of the active-site metal in terms of maintaining a native fold. Both His-brace occlusion and disorder are likely to interfere with oligosaccharide binding. Nonetheless, complexes were obtained with two oligosaccharides, although they do not interact with the His brace. These complexes might simply be crystal artefacts. However, owing to the unusual nature of LPMO binding surfaces and the unknowns regarding the natural substrates of AA13, it is also possible that these sites represent unusual SBS or binding sites for branched substrates. Further strategies on obtaining biologically relevant complexes with *Ao*AA13 will have to take into account the effects of metal ions in the packing of the so far only observed crystal form of the enzyme, and also consider the possible effects of long-term storage on the crystallized conformations.

Acknowledgements

This work was supported by a grant from the European Research Agency Industrial Biotechnology Initiative as financed by the Danish Council for Strategic Research (grant Nos. 12-134923 and 12-134922). The Danish Ministry of Higher Education and Science through the Instrument Center DANSCATT and the European Community's Seventh Framework Programme (FP7/2007–2013) under BioStruct-X (grant agreement No. 283570) funded travel to synchrotrons. We also would like to acknowledge MAX-lab, Sweden and the ESRF, France for synchrotron beamtime and assistance during data collection. Pernille von Freiesleben (Novozymes A/S), Dorthe Boelskifte (University of Copenhagen) and Katrine Rasmussen (University of Copenhagen) are thanked for technical assistance. The CESBIC consortium, in particular Professor Paul Walton (University of York), is thanked for helpful discussions on LPMOs.

References

Aachmann, F. L., Sorlie, M., Skjak-Braek, G., Eijsink, V. G. H. & Vaaje-Kolstad, G. (2012). *Proc. Natl Acad. Sci. USA*, **109**, 18779–18784.
Beeson, W. T., Phillips, C. M., Cate, J. H. & Marletta, M. A. (2012). *J. Am. Chem. Soc.* **134**, 890–892.
Bennati-Granier, C., Garajova, S., Champion, C., Grisel, S., Haon, M., Zhou, S., Fanuel, M., Ropartz, D., Rogniaux, H., Gimbert, I., Record, E. & Berrin, J.-G. (2015). *Biotechnol. Biofuels*, **8**, 90.
Borisova, A. S., Isaksen, T., Dimarogona, M., Kognole, A. A., Mathiesen, G., Várnai, A., Røhr, Å. K., Payne, C. M., Sørlie, M., Sandgren, M. & Eijsink, V. G. H. (2015). *J. Biol. Chem.* **290**, 22955–22969.
Chaplin, A. K., Wilson, M. T., Hough, M. A., Svistunenko, D. A., Hemsworth, G. R., Walton, P. H., Vijgenboom, E. & Worrall, J. A. (2016). *J. Biol. Chem.* **291**, 12838–12850.
Chiu, E., Hijnen, M., Bunker, R. D., Boudes, M., Rajendran, C., Aizel, K., Oliéric, V., Schulze-Briese, C., Mitsuhashi, W., Young, V., Ward, V. K., Bergoin, M., Metcalf, P. & Coulibaly, F. (2015). *Proc. Natl Acad. Sci. USA*, **112**, 3973–3978.
Christiansen, C., Abou Hachem, M., Janeček, Š., Viksø-Nielsen, A., Blennow, A. & Svensson, B. (2009). *FEBS J.* **276**, 5006–5029.
Cockburn, D., Wilkens, C., Ruzanski, C., Andersen, S., Willum Nielsen, J., Smith, A. M., Field, R. A., Willemoës, M., Abou Hachem, M. & Svensson, B. (2014). *Biologia*, **69**, 705–712.
Collaborative Computational Project, Number 4 (1994). *Acta Cryst.* D**50**, 760–763.
Courtade, G., Wimmer, R., Røhr, Å. K., Preims, M., Felice, A. K. G., Dimarogona, M., Vaaje-Kolstad, G., Sørlie, M., Sandgren, M., Ludwig, R., Eijsink, V. G. H. & Aachmann, F. L. (2016). *Proc. Natl Acad. Sci. USA*, **113**, 5922–5927.
Cuyvers, S., Dornez, E., Delcour, J. A. & Courtin, C. M. (2012). *Crit. Rev. Biotechnol.* **32**, 93–107.
Debreczeni, J. É. & Emsley, P. (2012). *Acta Cryst.* D**68**, 425–430.
Dhar, D. & Tolman, W. B. (2015). *J. Am. Chem. Soc.* **137**, 1322–1329.
Emsley, P. & Cowtan, K. (2004). *Acta Cryst.* D**60**, 2126–2132.
Emsley, P., Lohkamp, B., Scott, W. G. & Cowtan, K. (2010). *Acta Cryst.* D**66**, 486–501.
Frandsen, K. E. H. & Lo Leggio, L. (2016). *IUCrJ*, **3**, 448–467.
Frandsen, K. E. H. *et al.* (2016). *Nature Chem. Biol.* **12**, 298–303.
Gagnon, N. & Tolman, W. B. (2015). *Acc. Chem. Res.* **48**, 2126–2131.
Gregory, R. C., Hemsworth, G. R., Turkenburg, J. P., Hart, S. J., Walton, P. H. & Davies, G. J. (2016). *Dalton Trans.* **45**, 16904–16912.
Gudmundsson, M., Kim, S., Wu, M., Ishida, T., Momeni, M. H., Vaaje-Kolstad, G., Lundberg, D., Royant, A., Stahlberg, J., Eijsink, V. G. H., Beckham, G. T. & Sandgren, M. (2014). *J. Biol. Chem.* **289**, 18782–18792.
Harris, P. V., Welner, D., McFarland, K. C., Re, E., Navarro Poulsen, J. C., Brown, K., Salbo, R., Ding, H., Vlasenko, E., Merino, S., Xu, F., Cherry, J., Larsen, S. & Lo Leggio, L. (2010). *Biochemistry*, **49**, 3305–3316.
Harris, P. & Wogulis, M. (2010). Patent WO/2010/059413.
Harris, P. & Wogulis, M. (2011). Patent US/2011/0283421.
Hemsworth, G. R., Henrissat, B., Davies, G. J. & Walton, P. H. (2014). *Nature Chem. Biol.* **10**, 122–126.
Hemsworth, G. R., Johnston, E. M., Davies, G. J. & Walton, P. H. (2015). *Trends Biotechnol.* **33**, 747–761.
Hemsworth, G. R., Taylor, E. J., Kim, R. Q., Gregory, R. C., Lewis, S. J., Turkenburg, J. P., Parkin, A., Davies, G. J. & Walton, P. H. (2013). *J. Am. Chem. Soc.* **135**, 6069–6077.
Isaksen, T., Westereng, B., Aachmann, F. L., Agger, J. W., Kracher, D., Kittl, R., Ludwig, R., Haltrich, D., Eijsink, V. G. H. & Horn, S. J. (2014). *J. Biol. Chem.* **289**, 2632–2642.
Janeček, Š., Svensson, B. & MacGregor, E. A. (2011). *Enzyme Microb. Technol.* **49**, 429–440.
Johansen, K. S. (2016). *Biochem. Soc. Trans.* **44**, 143–149.
Johansen, K. S., Xu, F., Walton, P., McBrayer, B., Lund, H. & Soong, C. L. (2012). Patent PCT/US2012/028594.
Kabsch, W. (2010). *Acta Cryst.* D**66**, 125–132.
Karkehabadi, S., Hansson, H., Kim, S., Piens, K., Mitchinson, C. & Sandgren, M. (2008). *J. Mol. Biol.* **383**, 144–154.
Kittl, R., Kracher, D., Burgstaller, D., Haltrich, D. & Ludwig, R. (2012). *Biotechnol. Biofuels*, **5**, 79.
Laskowski, R. A., MacArthur, M. W., Moss, D. S. & Thornton, J. M. (1993). *J. Appl. Cryst.* **26**, 283–291.
Lee, J. Y. & Karlin, K. D. (2015). *Curr. Opin. Chem. Biol.* **25**, 184–193.
Levasseur, A., Drula, E., Lombard, V., Coutinho, P. M. & Henrissat, B. (2013). *Biotechnol. Biofuels*, **6**, 41.
Li, X., Beeson, W. T. IV, Phillips, C. M., Marletta, M. A. & Cate, J. H. D. (2012). *Structure*, **20**, 1051–1061.
Lo Leggio, L. *et al.* (2015). *Nature Commun.* **6**, 5961.
Lo Leggio, L., Welner, D. & De Maria, L. (2012). *Comput. Struct. Biotechnol. J.* **2**, 1–8.
Lombard, V., Golaconda Ramulu, H., Drula, E., Coutinho, P. M. & Henrissat, B. (2014). *Nucleic Acids Res.* **42**, D490–D495.
Morris, A. L., MacArthur, M. W., Hutchinson, E. G. & Thornton, J. M. (1992). *Proteins*, **12**, 345–364.
Murshudov, G. N., Skubák, P., Lebedev, A. A., Pannu, N. S., Steiner, R. A., Nicholls, R. A., Winn, M. D., Long, F. & Vagin, A. A. (2011). *Acta Cryst.* D**67**, 355–367.
Nekiunaite, L., Isaksen, T., Vaaje-Kolstad, G. & Abou Hachem, M. (2016). *FEBS Lett.* **590**, 2737–2747.
Newman, J. (2004). *Acta Cryst.* D**60**, 610–612.

Quinlan, R. J. *et al.* (2011). *Proc. Natl Acad. Sci. USA*, **108**, 15079–15084.
Scott, B. R., Huang, H. Z., Frickman, J., Halvorsen, R. & Johansen, K. S. (2016). *Biotechnol. Lett.* **38**, 425–434.
Vaaje-Kolstad, G., Bøhle, L. A., Gåseidnes, S., Dalhus, B., Bjørås, M., Mathiesen, G. & Eijsink, V. G. H. (2012). *J. Mol. Biol.* **416**, 239–254.
Vaaje-Kolstad, G., Houston, D. R., Riemen, A. H. K., Eijsink, V. G. H. & van Aalten, D. M. F. (2005). *J. Biol. Chem.* **280**, 11313–11319.
Vaaje-Kolstad, G., Westereng, B., Horn, S. J., Liu, Z., Zhai, H., Sorlie, M. & Eijsink, V. G. H. (2010). *Science*, **330**, 219–222.
Vaguine, A. A., Richelle, J. & Wodak, S. J. (1999). *Acta Cryst.* D**55**, 191–205.
Vu, V. V., Beeson, W. T., Span, E. A., Farquhar, E. R. & Marletta, M. A. (2014). *Proc. Natl Acad. Sci. USA*, **111**, 13822–13827.
Walton, P. H. & Davies, G. J. (2016). *Curr. Opin. Chem. Biol.* **31**, 195–207.
Winn, M. D. *et al.* (2011). *Acta Cryst.* D**67**, 235–242.